In-depth study of the formation processes of single atmospheric particles in the southeastern margin of Tibetan Plateau

Li Li[1,3], Qiyuan Wang[1,2], Jie Tian[1], Huikun Liu[1], Yong Zhang[1], Steven Sai Hang Ho[4], Weikang Ran[1], Junji Cao[5]

[1] Key Laboratory of Aerosol Chemistry and Physics, State Key Laboratory of Loess and Quaternary Geology, Institute of Earth Environment, Chinese Academy of Sciences, Xi'an 710061, China

[2] CAS Center for Excellence in Quaternary Science and Global Change, Xi'an 710061, China

[3] University of Chinese Academy of Sciences, Beijing 100049, China

[4] Division of Atmospheric Sciences, Desert Research Institute, Reno, NV 89512, United States

[5] Institute of Atmospheric Physics, Chinese Academy of Sciences, Beijing 100029, China

Correspondence to: Qiyuan Wang (wangqy@ieecas.cn) and Junji Cao (jjcao@mail.iap.ac.cn).

Abstract

The unique geographical location of the Tibetan Plateau (TP) plays an important role in regulating global climate change, but the impacts of the chemical components and atmospheric processing on the size distribution and mixing state of individual particles are rarely explored in the southeastern margin of the TP, which is a transport channel for pollutants from Southeast Asia to the TP during the pre-monsoon season. Thus a single-particle aerosol mass spectrometer (SPAMS) was deployed to investigate how the local emissions of chemical composition interact with the transporting particles and assess the mixing state of different particle types and secondary formation in this study. The TP particles were classified into six main types: the rich-potassium (rich-K) type was the largest fraction of the total particles (30.9%), followed by the biomass burning (BB) type (18.7%). Most particle types were mainly transported from the surroundings of the sampling site and Sino-Myanmar border; but the air masses from northeastern India and Myanmar show a greater impact on the number fraction of BB (31.7%) and Dust (18.2%) types, respectively. Then, the two episodes with high particle concentrations showed that the differences in the meteorological conditions in the same trajectory clusters could cause significant changes in chemical components, especially the Dust and EC-aged types, which changed by a sum of 93.6% and 72.0%, respectively. Ammonium and Dust particles distribute at a relatively larger size (~ 600 nm), but the size peak of other types is present at ~ 440 nm. Compared with the abundant sulfate ($^{97}HSO_4^-$), the low nitrate ($^{62}NO_3^-$) internally mixed in TP particles is mainly due to the fact that nitrate is more volatilized during the transport process. The formation mechanism of secondary speciation demonstrate that the formation capacity of atmospheric oxidation is presumably affected by the convective transmission and the regional transport in TP. However, the relative humidity (RH) could significantly promote the formation of secondary species, especially $^{97}HSO_4^-$ and $^{18}NH_4^+$. This study provides insights that can improve the knowledge of particle composition and size, mixing state, and aging mechanism at high time resolution over the TP region.

1 Introduction

Atmospheric aerosols have complex components and sources and can be coated with inorganic or organic materials during transport and atmospheric processing (Crippa et al., 2013). After further coating through coagulation, condensation and photochemical oxidation, its sizes, chemical compositions, mixing states and optical properties would change greatly, leading to its influence in the atmosphere more uncertain (Jacobson, 2002; Zaveri et al., 2010; Matsui, 2016; Budisulistiorini et al., 2017; Ma et al., 2012). Currently, the influences of the complex chemical components on aerosol size and mixing state show large regional differences due to the variations in the pollution sources, atmospheric formation mechanism and meteorological conditions, which have been widely studied in an urban area at a low altitude (Pratt et al., 2011; Liu et al., 2020a; Xu et al., 2017; Wang et al., 2022). However, previous study found that the migration or formation of low-volatile component (such as nitrate and organic matter) could effectively be reduced due to evaporation during the upward transportation process (Liu et al., 2020b), which further alter the chemical compositions and the particle sizes. The transportation of the aerosols to a relatively cleaner environment prevails the formation of secondary chemicals at a high altitude (Liu et al., 2020b). Therefore, a comprehensive investigation of the detailed characteristic of aerosol formation and mixing states is required to understand their environmental effects in low-, and high-altitude.

As a typical high-altitude region, the Tibetan Plateau (TP) has the highest and largest mountain area in the world, which is the most sensitive and obvious indicator of climate change in the entire Asian continent (Liu et al., 2017; Chen and Bordoni, 2014; Immerzeel et al., 2010). In recent decades, many studies have shown that the melting and retreat of glaciers in the TP regions is accelerating, and the main reason is attributable to anthropogenic emissions, such as greenhouse gases and aerosols (Luo et al., 2020; Hua et al., 2019). Atmospheric aerosols also can act as cloud condensation nuclei to impact the local hydrological cycles and monsoon patterns by changing the microphysical properties and life span of clouds (Qian et al., 2011; Gettelman et al., 2013; Kumar et al., 2017). The southern part of the TP is always affected by the transport of more polluted air from South Asia along the mountain valleys, especially during the pre-monsoon (i.e., March-May) with the

southwest prevailing wind (Chan et al., 2017; Zhao et al., 2017; Han et al., 2020). Most studies have focused on the optical characteristics within the TP; however, only a few research has been conducted on aerosol components.

Present aerosol components studies conducted in TP mostly focus on exploring the influence of light-absorbing carbon aerosols and dust particles on climate change by optical or offline sampling methods (e.g., Wang et al., 2019a; Liu et al., 2021). There is a lack of studies on the chemical composition, mixing states, and formation mechanism of aerosols in the southeast margin and even the entire TP, especially using high-time resolved measurements. Although time-integrated sampling with filter collection followed by laboratory analyses has been widely adopted for the chemical characterization of aerosols (Li et al., 2022a; Shen et al., 2015; Zhang et al., 2013). Drawbacks of the traditional approach include low time resolution, high detection limit, and time- and labor-intensive procedures. More advanced aerosol online measurement equipment with high-time resolution, such as the aerosol chemical speciation monitor (ACSM) and aerosol mass spectrometer (AMS) (Ng et al., 2011; Canagaratna et al., 2007) are mainly used to achieve online observation datasets of non-refractory submicron aerosol (including the mass concentration of sulfate, nitrate, ammonium, chloride, and organic; and their corresponding mass spectral). This is beneficial to recognize the dynamic processes of source emission in the atmosphere (Du et al., 2015; Zhang et al., 2019a). At the same time, aerosol time-of-flight mass spectrometry (ATOFMS) (Dall'Osto et al., 2014), and single particle aerosol mass spectrometer (SPAMS) (Zhang et al., 2020), are popular for characterizing atmospheric individual particles. These devices can determine the chemical composition and size distribution of the particles in detail, such as the dynamic processes of chemical aging, mixing state, and transport of the aerosols (Liang et al., 2022; Li et al., 2022b; Zhang et al., 2019b). To the best knowledge, the advanced measurement device has not yet been applied for the studies conducted in TP, leading to a lack of in-depth research on the $PM_{2.5}$ pollution in TP, especially in the southeastern margin, which hinders our understanding of the distribution characteristics and formation mechanism of aerosol components in high-altitude regions.

The southeastern margin of the TP is an important transitional zone between the high-altitude TP and the low-altitude Yungui Plateau (Wang et al., 2019a; Zhao et al., 2017),

103 an ideal place for investigating the impacts of pollutants transport and formation in the

104 high-altitude zone. In this study, continuous field observation of individual particles (SPAMS)

105 was deployed on the southeastern margin of the TP during the pre-monsoon period, to (i)

106 investigate the changes of chemical characteristics between transport and local fine particles

107 during pre-monsoon, (ii) determine the particle size distributions, and the mixing states of

108 different particle types, and (iii) assess the contributions of photooxidation and aqueous

109 reaction to the formation of the secondary species. These results would expand our

110 understanding of the chemical components, size distribution, mixing state, and aging

111 pathways of aerosols in the high-altitude areas in the TP and surrounding areas.

112 **2   Methodology**

113 **2.1 Sampling site**

114 Intensive 1-month field observation was deployed at the rooftop ($\sim$ 10 m above ground

115 level) of the Lijiang Astronomical Station, Chinese Academy of Sciences (3260 m above sea

116 level; 26°41′24″N, 100°10′48″E), Gaomeigu County, Yunnan Province, China, during the

117 pre-monsoon period (from April 14th to May 13th, 2018). The nearest residential area is the

118 Gaomeigu village (3–5 km away) with a small population size of 113 residents in 27

119 households. Villagers earn a living by farming (e.g., potato and autumn rape), and biomass is

120 the major domestic fuel (Li et al., 2016). The site is surrounded by rural and mountainous

121 areas and has no obvious industry or traffic emissions. During the observation period, the

122 average temperature (T) and relative humidity (RH) are 8.4 $\pm$ 3.1℃ and 69% $\pm$ 21%,

123 respectively. The wind speed (WS) is 2.2 $\pm$ 1.2 m·s^{-1} with the prevailing wind in the north and

124 northeastern (Fig. S1).

125 **2.2 On-line instrument**

126 A detailed operational principle and the calibrations of the single-particle aerosol mass

127 spectrometer (SPAMS, Hexin Analytical Instrument Co., Ltd., Guangzhou, China) has been

128 described elsewhere (Li et al., 2011). Briefly, individual particles are drawn into SPAMS

129 through a critical orifice. The particles are focused and accelerated, then aerodynamically

130 sized by two continuous diode Nd: YAG laser beams (532 nm), subsequently desorbed and

131   ionized by a pulsed laser (266 nm) triggered exactly based on the velocity of the specific

132   particle. The generated of positive and negative molecular fragments are recorded with the

133   corresponding size of individual particles. In summary, a velocity, a detection time, and an

134   ion mass spectrum are recorded for each ionized particle, while there is no mass spectrum for

135   not ionized particles. The velocity could be converted to d_{va} based on a calibration using

136   polystyrene latex spheres (PSL, Thermo Scientific Corp., Palo Alto, USA) with predefined

137   sizes. The average ambient pressure is 690 hPa (in a range of 685–694 hPa) during the

138   measurements and calibration. Particles measured by SPAMS mostly are within the size

139   range of vacuum aerodynamic diameter (d_{va}) 0.2–2.0 µm. A hollow silicone dryer was

140   installed in front of the inlet. This reduces the uncertainty of particle collection efficiency due

141   to the changes of humidity in sampled airs.

142   Meteorological parameters, including the planetary boundary layer (PBL), temperature

143   (℃), RH (%), WS (m·s^{-1}), and wind direction (WD) were continuously achieved using an

144   automatic weather station (Model MAWS201, Vaisala HydroMet, Helsinki, Finland) at a time

145   resolution of 5 min. Gaseous concentrations (ppbv) were obtained using a multiple gas

146   analyzer (Thermo Scientific Corp.), including ozone (O_3, model 49i) and nitrogen oxides

147   (NO_x, model 42i) in a 5-min resolution. The SPAMS and gas analyzers are co-located in the

148   same position, while the weather station was uncovered outside ~5 m from the sampling

149   house. Time series of SPAMS particles, gaseous concentrations (NO, NO_x, O_3, and CO) and

150   meteorological parameters (PBL, temperature, RH, WD, and WS) were shown in Fig. S2.

151   **2.3 Individual particle classification**

152   During the observation period, a total of 461,876 ambient particles with the size (d_{va}) of

153   0.2–2.0 µm were collected, including 55,583 in Episode I (E1; from April 18th 08:00 local

154   time (LT) to April 19th 08:00 LT) and 62,110 in Episode II (E2; from April 26th 17:00 LT to

155   April 28th 02:00 LT). The analyzed particles are classified into 1,557 groups using an adaptive

156   resonance theory neural network (ART-2a) with a vigilance factor of 0.8, a learning rate of

157   0.05, and 20 iterations (Song et al., 1999). Finally, eight major particle clusters [i.e.,

158   potassium-rich (rich-K), biomass burning (BB), organic carbon (OC), Ammonium, aged

159   element carbon (EC-aged), Dust, sodium (Na)-potassium (K)-containing (NaK-SN), and iron

160 (Fe)-lead (Pb)-containing (Metal)] with distinct chemical patterns were manually combined,

161 which represent ∼99.7 % of the population of the detected particles. The remaining particles

162 are grouped as "Other". The characteristics of the positive and negative mass spectra (MS) of

163 each particle type are shown in Fig. S3. A detailed description of classification criteria for

164 individual particles and the characteristic ion fragments for each particle type can be found in

165 Text S1. The criteria used for searching the some secondary species in the SPAMS datasets

166 are summarized in Table S2.

2.4 Trajectory-related analysis

168   To determine the influence of regional transport on different particles at Gaomeigu, the

169 trajectory clusters analysis was carried out using the 72-h backward air mass trajectories at

170 arrival heights of 500 m above ground level. The trajectories were calculated with the Hybrid

171 Single-Particle Lagrangian Integrated Trajectory model (Draxler and Hess, 1998), and the

172 meteorological data were obtained from the Global Data Assimilation System (GDAS;

173 ftp://arlftp.arlhq.noaa.gov/pub/archives/gdas1, last access: 6 April, 2022). The cluster analysis

174 employs a Euclidean-oriented distance definition to differentiate and cluster the major spatial

175 features of the inputting trajectories. Details of the trajectory clustering method can be found

176 in Sirois and Bottenheim (1995). To investigate the effects of transport on the chemical

177 characteristic of the individual particles, trajectories with particle number concentrations high

178 than the 75th percentile are considered as pollution (Liu et al., 2021).

3   Results and Discussion

3.1 Characteristics of particle composition

181   Table 1 summarizes the numbers of concentrations, relative percentages, and

182 characteristic ions of each particle type. The most dominant particle type in Gaomeigu during

183 pre-monsoon is rich-K, accounting for an average of 30.9% of the total resolved particles,

184 followed by BB (18.7%), OC (12.8%), Ammonium (11.9%), EC-aged (10.9%), and Dust

185 (10.7%). Similar to the results of some studies in urban areas, rich-K or

186 carbonaceous-containing type is the dominant particle type (15-50%) (Xu et al., 2018; Wang

187 et al., 2019b; Li et al., 2022). The difference is that few researchers can capture the high

188 proportion of Ammonium particles as shown in this study (Shen et al., 2017; Xu et al., 2018),

189 which is ascribed to the conversion of ammonia (NH_3) precursor emitted from large-scale

190 agricultural activities and mountain forest (Engling et al., 2011; Li et al., 2013). It is

191 necessary to point out that 60% of Ammonium particles contain signals of amine fragment

192 (m/z 58, $C_2H_5NH=CH_2^+$), implying their similar formation pathway (Zhang et al., 2012).

193 Moreover, the amine-containing particle represented 12.5% of the total ambient particles,

194 which is significantly higher than that in some urban areas at low altitudes (around 2%) (Cahi

195 et al., 2012; Zhang et al., 2015; Li et al., 2017) but is comparable to that at observed sites

196 with high RH, or during fog and cloud events at a high altitude (> 9%) (Roth et al., 2016; Lin

197 et al., 2019). This suggests that the formation of amines under high RH and fog conditions

198 might exist in the Gaomeigu area (with an altitude of 3260 m), for example, the high relative

199 fraction of amine-containing particle corresponds to a high RH (Fig. S4), and the existence of

200 amine sources govern the ammonium formations (Bi et al., 2016; Rehbein et al., 2011). The

201 relatively larger fraction of Dust particles is related to the short-time occurrences of dust

202 events in spring (Fig. S5), leading to a wide contribution ranging between 10% and 70% in

203 the period of 19:00 LT on April 16th to 10:00 LT on April 17th.

204 Fig. 1 shows the diurnal variations of each particle type. The rich-K, BB, and OC

205 particles decrease after midnight until 06:00 LT, possibly explained by the curtailment of

206 local traffic and biomass-burning activities at nighttime even though both the planetary

207 boundary layer (PBL) height and WS decrease (Fig. S6). Then, their intensities rapidly

208 increase in the morning (around 07:00 LT) due to more pollutants from biomass burning and

209 traffic emissions at the upwind region. The increases of PBL height and WS also lead to the

210 air pollutants transported from the surrounding environment to the sampling site (Liu et al.,

211 2021). At 11:00 LT, the particle counts sharply decrease till 16:00–17:00 LT, caused by the

212 pollutant dispersion with the increases of the PBL height and WS. Increasing trends are

213 observed after 17:00 LT due to the reduction of PBL height and WS. In contrast, the

214 Ammonium, EC-aged, and Dust particles show a unimodal pattern of the daily diurnal

215 variation (Fig. 1d–f). From 00:00 to 06:00 LT, minor fluctuation of particle concentrations of

216 Ammonium, EC-aged, and Dust is observed for these particle types. After that, their levels

217 continuously elevate until ~11:00 LT due to the regional transport, traffic emission, and

fugitive dust (Text S2). While the PBL height and WS increase continuously, the Ammonium, EC-aged, and Dust particles begin to decline from 12:00 to 17:00 LT. The subsequent increases of these three particles after 17:00 LT are attributed to the reduction of PBL height, as a result of the accumulation of pollutants in the near-surface atmosphere.

Based on the transport pathways, four air mass clusters are identified to investigate the effect of regional transport on the major particle types (i.e., rich-K, BB, OC, Ammonium, EC-aged, and Dust) (Fig. 2). Cluster 1, 3 and 4 originated from northeastern Myanmar,, accounting for 59.8%, 33.2% and 4.6% of the total trajectories, respectively. Cluster 1 had an average percentage of 32.7%, 18.5%, 12.0%, 12.5%, 11.1%, and 8.9%, respectively, on the rich-K, BB, OC, Ammonium, EC-aged, and Dust particles (Table S1). Clusters 3 and 4 have comparable contributions of BB, OC, Ammonium, and EC-aged to those of Cluster 1, but with a high contribution of Dust, which approximately 16.6% of Clusters 3 and 4 are referred to as dust pollution. The diurnal variations of the BB and OC fractions are similar which rapidly elevate at 07:00 LT (Fig. S7) due to the increased contribution of biomass burning and vehicle emissions from Cluster 1, Ammonium and EC-aged particles (peak at 07:00 LT) caused by the effect of Cluster 1 and 3 together. The similar diurnal trend of Clusters 3 and 4 are both associated with dust contributions, which decrease at 04:00 LT and increase at noon. The increased nighttime particles could be attributed to the pollutant accumulation with the decreased PBL height. Cluster 2 originate from northeastern India and passes over Bangladesh. This cluster accounts for only 2.4 % of the total trajectories, in which ~30.8% and ~35.9% are mainly associated with the rich-K and BB particles, respectively. Even though Clusters 2 and 4 are composed of a small fraction of total trajectories (2.4% and 4.6 %, respectively), BB and dust particles are identified as the major pollutants, suggesting significant influences from India and northeastern Myanmar during the campaign.

A more in-depth investigation of the characteristics of the main particle types in the southeastern Tibet Plateau was conducted during two episode periods when the number concentration of particles was high (i.e., E1: from 08:00 LT April 18th to 08:00 LT April 19th, 2018; E2: 17:00 LT April 26th to 02:00 LT April 28th, 2018) (Fig. S5). Even though the two episodes are contributed by Cluster 1, the chemical components show significant differences

247   (Table 1). During E1, the average fractions of the rich-K, BB, OC, Ammonium, EC-aged, and

248   Dust particle are 29.0%, 11.5%, 8.1%, 17.5%, 10.0% and 20.3%, respectively, different from

249   39.3%, 14.2%, 10.0%, 13.5%, 17.2%, and 1.3% respectively, during E2. It can be seen that

250   the Dust particle is the major changed factor, which is 93.6% lower during E2 than E1,

251   whereas the EC-aged particle shows a reversible of 72.0% higher during E2. The rich-K, BB,

252   and, OC particles show 22.9%-35.5% differences between the two episode periods. For the

253   air mass clusters (Fig. S8), E1 and E2 exhibit minor differences, mostly originating from

254   northern Myanmar and the Sino-Burmese border, but not identical regions. The Dust particles

255   that are much lower during E2 than E1 could be explained by higher WS (on average of $2.7 \pm$

256   1.0 m/s versus 0.4 ± 0.5 m/s) (Fig. S8) and PBL height (771 ± 717 m versus 560 ± 549 m)

257   (Fig. S9). The Dust particles are mainly formed by re-suspension in the local areas. In

258   addition, the quick thrown-up dust belongs to more coarse size particles, which are out of the

259   detection range of the SPAMS. However, due to the larger dust particles deposited more

260   easily under the low WS and the stagnant air conditions during E1, more suspended dust

261   particles of small size fall in the detection range of SPAMS. Moreover, the increased PBL

262   height and WS could speed up the transportation of pollutants from multiple sources (e.g.,

263   traffic and biomass burning emissions) to the observation site, leading to elevate the fraction

264   of EC-aged, rich-K, BB, and OC particles. The decreased Ammonium particle during E2 is

265   potentially explained by the reductions in the secondary pollutant formation with declines of

266   RH (from $73.9\% \pm 23.9\%$ to $53.1\% \pm 14.9\%$), the oxidation capacities [O_3: from 82.3 ± 5.5

267   ppbv to 76.8 ± 8.4 ppbv; and NO_x: from, 3.9 ± 0.8 to 2.7 ± 0.8 ppb), in comparison to those

268   during E1.

269   **3.2 Characteristics of size distribution and mixing state**

270   The aerodynamic size distributions of all particle types are shown in Fig. 3. According to

271   the characteristics of the average MS (Text S1 and Fig. S3), rich-K, BB, and OC and EC-aged

272   particles originated from the similar sources of vehicle emission or solid-fuel combustion.

273   Their size distribution thus presents within a small-scale (~440 nm) (Fig. 3a). However, the

274   relative percentage of each particle type is distinct with different size ranges, possibly due to

275   the unique atmospheric processing. For example, as shown in Fig. 3b, the proportions of

276 rich-K and BB types increases along with the increase in particle size from 200 to 420 nm but

277 then decrease. OC and EC-aged types are mainly distributed in relatively small particle sizes,

278 and their proportions gradually decrease when the size ranges become lager. Ammonium and

279 Dust types are mainly distributed in large sizes of ~600 nm (Fig. 3a). The proportion of

280 Ammonium particles gradually increases with the increase of particle size and peaks at 740

281 nm, the relatively large size distribution is ascribed to the intense atmospheric aging during

282 regional transport (Text S1). The proportion of Dust particles gradually increases with a

283 size > 560 nm and peaks at 1.48 μm. This is consistent with the fact that dust is a coarse

284 particle, generally formed at the roadside and fly ash.

285   Compared with the total particle size distribution, the peak values of the six main

286 particle types show minor differences (< 80 nm) during the two different episode periods (Fig.

287 S10a). In Fig. S10b, a relatively high proportion of the rich-K and BB particles exhibit

288 bimodal distributions, while peaks at < 300 nm are affected by the primary emissions and >

289 300 nm are associated with the aging process (Li et al., 2022b; Bi et al., 2011). Hence, the

290 percentage of the six particle types distribute in wider size ranges during E2 than during E1

291 due to the more intensive atmospheric aging. Relatively greater fluctuation for the large-size

292 fractions (> 1.1 μm) could be explained by the low particle concentration (a number less than

293 20). It should be pointed out that further application of this method would require a

294 co-located particle-sizing instrument to scale the size-resolved particle detection efficiency.

295 Both particle composition and size-dependent are the predominant impacting factors on the

296 particle detection efficiency of the SPAMS (Wenzel et al., 2003; Yang et al., 2017; Healy et

297 al., 2013).

298   To investigate the mixing state of the secondary species in the six main particle types,

299 the number fractions of six secondary markers ($^{97}HSO_4^-$, $^{195}H(HSO_4)_2^-$, $^{62}NO_3^-$, $^{18}NH_4^+$,

300 $^{58}C_2H_5NHCH_2^+$ and $^{89}HC_2O_4^-$) are selected (Fig. 4). The presences of amine (*m/z*

301 $^{58}C_2H_5NHCH_2^+$) and sulfuric acid (*m/z* $^{195}H(HSO_4)_2^-$) signals are possibly indicative of the

302 water uptake (Chen et al., 2019) and acidic property of the particles (Rehbein et al., 2011),

303 respectively. The mixing states are calculated by the ratio of the number concentration of the

304 selected ions to each particle type.

305   The most abundant of $^{97}HSO_4^-$ and $^{18}NH_4^+$ fraction are seen in Ammonium (99% and

94%, *respectively*) and EC-aged (92% and 31%, *respectively*) particles, whereas much low fraction of $^{62}NO_3^-$ is found (2% and 7%, *respectively*). These suggest that ammonium sulfate is not a predominant form instead of ammonium nitrate (Zhang et al., 2013). The high contribution of sulfate in EC-containing particles also suggests a significant influence of anthropogenically emitted sulfate precursors (e.g., SO_2) on the aging of EC-containing particles at the high altitude (Peng et al., 2016; Zhang et al., 2017a). Meanwhile, relatively high number fractions of $^{195}H(HSO_4)_2^-$ and $^{58}C_2H_5NHCH_2^+$ are also observed in Ammonium (63% and 60%) and EC-aged (4% and 19%) particles. These abundant mixtures potentially represent the high hygroscopicity of Ammonium and EC-aged particles, and their ability to neutralize the acidic particles of Ammonium particle (Sorooshian et al., 2007). Then, a moderate fraction of $^{97}HSO_4^-$ and $^{18}NH_4^+$ are seen on the rich-K (65%, 7%) and OC (56%, 4%) particles. In contrast, more $^{62}NO_3^-$ contribute to the rich-K (38%) and OC (68%) particles, mainly affected by vehicle emissions (Text S1). Following BB (18%) and Dust (6%) particles are found in a relatively low number fraction of $^{97}HSO_4^-$, while the moderate $^{62}NO_3^-$ accounts for 45% of the BB particle but only 3% of the Dust particle. Besides, the number fraction of $^{18}NH_4^+$ is minor (＜1%), which suggests the aging degree of BB and Dust particles is relatively low. In addition, oxalate ($^{89}HC_2O_4^-$), a representative component of secondary organic formation is mainly mixed with BB (13%) and rich-K (12%) particles. This is because the substantial precursors of oxalic acid, including acetate ($^{59}C_2H_3O_2^-$), methylglyoxal ($^{71}C_3H_3O_2^-$), glyoxylate ($^{73}C_2HO_3^-$), are emitted from biomass burning, while oxalate heterogeneously formed in BB related particles (Zhang et al., 2019b; Zauscher et al., 2013). A relatively low fraction (<5%) of the oxalate-containing particles in OC, Ammonium, EC-aged and Dust particles potentially limited by the contributions of precursor oxalic acid.

Compared to the individual particle mixing state in urban or suburban areas that are located close to emission sources (Chen et al., 2016; Dall′Osto and Harrison, 2012; Zhang et al., 2017a; Li et al., 2022b), the high fractions of sulfate and ammonium at the high altitude area demonstrate a high degree of aging of the individual particles, whereas the low fraction of nitrate with high volatility indicates its loss during transportation processing.

The number fractions of six markers in the four clusters were used to further investigate the impacts of regional transport. As shown in Fig. 5a and c, the dominant mixing ion types in

336   each particles (except for Dust type) are similar among the four Clusters. For Cluster 1, the

337   number fractions of $^{97}HSO_4^-$ and $^{89}HC_2O_4^-$ have larger values in five particle types (except

338   for Dust type) than those in other clusters. Similar to Cluster 1, 3 and 4 are impacted by

339   regional transport from northeastern Myanmar. Moreover, the fractions of the six markers are

340   similar in in OC, Ammonium, and EC-aged types. However, $^{97}HSO_4^-$ is decreased in rich-K,

341   BB and Dust types, while $^{62}NO_3^-$ is increased in rich-K and decreased in Dust types. As

342   discussed in Section 3.1, these phenomena demonstrate that the aging degree of Cluster 3 and

343   4 might be lower than that of Cluster 1. For Cluster 2, the fraction of $^{97}HSO_4^-$ is obviously

344   decreased in rich-K, BB and EC-aged types but slightly increased in Dust type (Fig. 5f). Such

345   pattern inverse the observations in rich-K, OC and Dust types for $^{62}NO_3^-$ ions. These

346   variations in Cluster 2 are more likely due to influences of biomass-burning activities from

347   the surrounding area of the sampling site, rather than regional transport. Furthermore, Cluster

348   2 is associated with regional transport from northeastern India along the afternoon to

349   nighttime (from 15:00 LT on 11 May to 07:00 LT on 12 May), which is favorable to the

350   nitrate formation N_2O_5 by heterogeneous hydrolysis (Wang et al., 2017; Ding et al., 2021).

351   However, these cases ae infrequent, as only 2% of trajectories are associated with Cluster 2.

352   During E1, more than 50% of $^{97}HSO_4^-$ fractions are mixed in the rich-K (81%), OC

353   (62%), Ammonium (100%), EC-aged (98%) particles (Fig. S11), lower than in BB (37%) and

354   Dust (4%) particles. Dissimilar with E1, the number fraction of $^{97}HSO_4^-$ increases to 34%

355   during E2, potentially associated with the enhancement by secondary formation. However,

356   the mixing state of $^{195}H(HSO_4)_2^-$), $^{62}NO_3^-$, NH_4^+ and oxalate fractions are similar between the

357   two episodes events. The fractions of $^{58}C_2H_5NHCH_2^+$ are significantly higher in E2 than E1

358   for Ammonium (67% versus 31%) and EC-aged particles (48% versus 17%), due to the

359   relatively higher hygroscopic behavior (i.e., RHs) (Sorooshian et al., 2007).

360   **3.3 Formation process of the high number concentration particle episodes**

361   Photochemical oxidation and aqueous-phase reaction are the key formation pathways of

362   secondary species (Link et al., 2017; Xue et al., 2014; Jiang et al., 2019). Generally, the

363   oxidant O_x (O_3 + NO_2) concentration and RH serve as indicators of the degree of

364   photochemical oxidation (Wood et al., 2010) and aqueous-phase reaction (Ervens et al., 2011).

365   In this study, the relative number fractions of $^{43}C_2H_3O^+$, $^{89}HC_2O_4^-$, $^{62}NO_3^-$, $^{97}HSO_4^-$, and

$^{18}NH_4^+$-containing particles to the total detected particles were selected to indicate the secondary formation (Liang et al., 2022). The correlations of the number fraction of each secondary species with the O_x concentrations (O_x) during daytime (from 06:00 to 20:00 LT) and RH during nighttime (from 20:00 to 06:00 next day LT) are used to present the formation pathways during the two episodes (Li et al., 2022).

As illustrated in Fig. 6, for E1, $^{43}C_2H_3O^+$, $^{89}HC_2O_4^-$, $^{97}HSO_4^-$, $^{18}NH_4^+$ show significant negative linear correlations with O_x ($p < 0.01$), and the correlation strengths range from moderate to strong (r = –0.51 to –0.81). However, the $^{62}NO_3^-$ fraction shows an upward trend with an insignificant correlation (r = 0.33, $p > 0.05$) with the increase in O_x concentration. For E2, $^{43}C_2H_3O^+$ shows weak correlation with O_x (r = 0.37, $p > 0.05$), but strong correlations with $^{89}HC_2O_4^-$, $^{97}HSO_4^-$, and $^{18}NH_4^+$ (r = 0.81~0.92, $p < 0.01$). It should be noted that $^{62}NO_3^-$ has a strong negative correlation (r =–0.85, $p < 0.01$) with O_x. In general, the opposite linear relationship between secondary aerosol and O_x during E1 and E2 might be influenced by reasons of i) the relatively low secondary formations because of the small amount of precursors emitting from anthropogenic activities around the sampling site (Li et al., 2016); ii) higher dilution rate of the particles formed in the atmosphere with the rapid rise of PBL height during E1 than E2 (Fig. S12a); iii) the degrees of contributions of regional transport due to the low WS (0.5 ± 0.6 m s^{-1}) during E1 and the high WS (3.1 ± 1.0 m s^{-1}) during E2, respectively (Fig. S8). Therefore, for E1, the increases of NO_3^- fraction could be influenced by the local nitrate formation, while the declines of other secondary components should be ascribed to the reduced contribution of regional transport. For E2, the decreased of NO_3^- fraction could be caused by the relatively higher volatilization loss of nitrate than other components through the regional transport. Previous study proves that the formations of organic nitrate species (such as $^{27}CHN^+$, $^{30}NO^+$, $^{43}CHO_1N^+$ and CHO_xN^+) through the NO+RO$_2$ pathway dominate 80% of the total nitrate production in tropical forested regions during summertime (Alexander et al., 2009). Aruffo et al (2022) also found that low NO_x (i.e. < 6 ppbv), compared to 2.3 ± 0.8 ppbv in this study, could even promote the particle-phase partitioning of the lower volatility of organonitrates. These results suggest that photo-oxidation reactions could promote secondary formation, among which the rate of HSO_4^- formation (slop=0.017) is the highest. Increased with O_x concentration during E2, the

396   concentration levels of secondary organic species of $C_2H_3O^+$ (18%-28%) imperceptibly rise,

397   while the oxalate fraction significantly increase by 7%-20% as well. The results indicate that

398   the secondary organic species have different formation capacities through atmospheric

399   oxidation.

400   Considering that the oxalate is abundant mixed in rich-K (14%), BB (15%), EC-aged

401   (5%), and Dust (6%) particles in Cluster 1 (Fig. 5), and the increased contributions of rich-K

402   (39.3%), BB (14.2%) and EC-aged (17.2%) types during E2 (Table 1), the apparent formation

403   of oxalate might be due to the enhancement of regional transport. Particularity, this presents

404   the nearby biomass burning and combustion activities produce more precursor species of

405   oxalate (Sullivan et al., 2007; Kundu et al., 2010; Zhang et al., 2017b).

406   Fig. 7 illustrates that the number fractions of $^{43}C_2H_3O^+$, $^{89}HC_2O_4^-$, $^{97}HSO_4^-$, and $^{18}NH_4^+$

407   have moderate to strong positive correlations with RH (r = 0.70~0.81, $p < 0.01$ or 0.05) in the

408   nighttime during the two episodes, except that $^{43}C_2H_3O^+$ during E2 ($p = 0.48$) and $^{89}HC_2O_4^-$

409   during E1 ($p = 0.12$). Furthermore, $^{62}NO_3^-$ fraction has no obvious changes with insignificant

410   correlation with RH during E1 ($p = 0.43$) and presents a moderate negative correlation with

411   RH (r = 0.69, $p < 0.01$) during E2. As shown in Fig. 7e, the highest aqueous formation rate of

412   HSO_4^- is mainly due to the properties of low volatile and high hygroscopic of sulfate (Wang

413   et al., 2016; Zhang et al., 2019c; Sun et al., 2013). Compared with that during E2

414   (slop=0.014), the decreased formation rate of HSO_4^- during the E1 (slop=0.009) may be

415   because the decreases of aerosol acidity in higher RH > 80% (Huang et al., 2019; Meng et al.,

416   2014; Tian et al., 2021). And the increased contributions of regional transport due to the high

417   WS (2.4 ± 0.8 m s^{-1}) during E2 are comparable to the low WS (0.08 ± 0.08 m s^{-1}) during E1

418   (Fig. S8). The fair production rate of NH_4^+ during the E1 (slop= 0.005) and E2 (slop=0.006)

419   demonstrate that an aqueous-phase reaction could effectively promote ammonium formation.

420   Meanwhile, a slightly larger slop during E2 could be also affected by the increased

421   contributions of regional transport. Compared with those during E1, the inverse generation

422   rates of two secondary organic species (i.e., $C_2H_3O^+$ and $HC_2O_4^-$) during E2 are possibly

423   caused by the different formation pathways with a variety of RH levels or distinct regional

424   transports. For example, $C_2H_3O^+$ shows a strong correlation with RH (r = 0.70, $p < 0.05$)

425   during E1 (slop=0.003) but has insignificant correlation during E2. This could be explained

426   by high RHs that could effectively promote secondary organic formation during E1. In

427   addition, the $HC_2O_4^-$ fraction increases slightly (9.7-13.1%) during E1 is potentially ascribed

428   to more abundant Dust-type particles (20.3%) which compose of high calcium (Ca) (Fig. S13)

429   that favor the formation of metal oxalate complexes (i.e., Ca oxalate). At high RHs (93.4 ±

430   7.6%), if oxalate ions are dissolved in the aqueous phase with the presence of Ca ions, the Ca

431   oxalate complexes can precipitate because of their low hygroscopic and insoluble natures

432   (Furukawa and Takahashi, 2011). This could offset the oxalate formation in the

433   aqueous-phase reaction. However, significant linear increases (slop=0.003) with RH (r = 0.81,

434      $p < 0.01$) during E2 demonstrate that the aqueous-phase reaction effectively promotes the

435   oxalate formation (Cheng et al., 2017; Meng et al., 2020). No obvious change and

436   insignificant correlation between $^{62}NO_3^-$ and RH are found during E1, potentially attributed

437   to the decreases of NO_2 concentration (3.7 ± 0.4 ppbv) in the local atmosphere. Meanwhile,

438   high RHs could promote organonitrates formation (Fang et al., 2021; Fry et al., 2014). The

439   linearity between $^{62}NO_3^-$ and RH (r = 0.69, $p < 0.01$) significantly decreases during E2,

440   mostly due to the losses of the volatile compound through the regional transport (Fig. S14).

441   **4   Conclusions**

442   This study presents the chemical composition, size distribution, mixing state, and

443   secondary formation of individual particles in the southeastern margin of TP, China during

444   the pre-monsoon season using a high-resolution SPAMS. The finding shows that the rich-K

445   (30.9%) and BB types (18.7%) are the two dominant aerosol particles in the remote area;

446   followed by the OC (12.8%), Ammonium (11.9%), EC-aged (10.9%), and Dust (10.7%) types;

447   the NaK-SN, Metal and Others types contributed 0.3–2.8% to the total ambient particles. By

448   interpreting the mass spectra and diurnal trends, the major particle types are mainly from

449   traffic emission, biomass burning, secondary formation, and fly ash, while the dynamics of

450   the PBL height could also affect the contributions of these particles. The observed change in

451   the number fraction of the particle types was mainly influenced by air mass (97.61% of the

452   total trajectories) from northeastern Myanmar, and significantly contributed to rich-K and BB

453   types. The particle types show distinct size distributions. The two most critical particle types

454   of rich-K and BB appear in a unimodal pattern, the fractions of OC and EC-aged gradually

455   decrease with the increase of the particle sizes, but Ammonium and Dust types show the

456 opposite. Sulfate is the major secondary species and is highly mixed with rich-K, Ammonium,

457 and EC-aged types. Nitrate has a relatively low mixing ratio due to its higher volatility than

458 sulfate during regional transportation, except for BB and OC types. During the entire study

459 campaign, two air episodes with the high number concentration particle occurred but with

460 significant differences in each particle fraction due to the different meteorological conditions

461 (RH, WS, etc.). The indicators of secondary formation, $C_2H_3O^+$, $HC_2O_4^-$, NH_4^+, NO_3^- and

462 HSO_4^- are shown inverse linear correlation with O_x (O_3+NO_2) during episode Ⅰ and Ⅱ

463 periods due to the different meteorological conditions; however, they are present a positive

464 linear correlation with relative humidity (RH), except for NO_3^- shown the negative linear

465 correlation with RH due to the low precursors concentration and potential organonitrates

466 formation. These results demonstrated that the capacity of atmospheric aging of

467 photo-oxidation and aqueous reaction have complex influencing factors. The results of this

468 study provide useful information concerning the detailed characteristic of aerosol components,

469 size distribution, and mixing states in the southeast TP, and highlight the importance of the

470 cross-border transport and formation mechanism of aerosols in high-altitude regions.

488

Reference

490 Alexander, B., Hastings, M. G., Allman, D. J., Dachs, J., Thornton, J. A., and Kunasek, S. A.: Quantifying
491   atmospheric nitrate formation pathways based on a global model of the oxygen isotopic composition
492   ($\Delta^{17}O$) of atmospheric nitrate, Atmos. Chem. Phys., 9, 5043–5056,
493   https://doi.org/10.5194/acp-9-5043-2009, 2009.
494 Aruffo, E., Wang, J., Ye, J., Ohno, P., Qin, Y., Stewart, M., McKinney, K., Di Carlo, P., and Martin, S. T.:
495   Partitioning of Organonitrates in the Production of Secondary Organic Aerosols from α-Pinene
496   Photo-Oxidation, Environ. Sci. Technol., 56, 5421–5429, https://doi.org/10.1021/acs.est.1c08380,
497   2022.
498 Bi, X. H., Zhang, G. H., Li, L., Wang, X. M., Li, M., Sheng, G. Y., Fu, J. M., and Zhou, Z.: Mixing state of
499   biomass burning particles by single particle aerosol mass spectrometer in the urban area of PRD,
500   China, Atmos. Environ., 45, 3447–3453, https://doi.org/10.1016/j.atmosenv.2011.03.034, 2011.
501 Bi, X. H., Lin, Q. H., Peng, L., Zhang, G. H., Wang, X. M., Brechtel, F. J., Chen, D. H., Li, M., Peng, P. A.,
502   Sheng, G. Y., and Zhou, Z.: In situ detection of the chemistry of individual fog droplet residues in the
503   Pearl River Delta region, China, J. Geophys. Res. Atmos., 121, 9105–9116,
504   https://doi.org/10.1002/2016jd024886, 2016.
505 Budisulistiorini, S. H., Riva, M., Williams, M., Chen, J., Itoh, M., Surratt, J. D., and Kuwata, M.:

Light-absorbing brown carbon aerosol constituents from combustion of Indonesian peat and biomass, Environ. Sci. Technol., 51, 4415-4423, https://doi.org/10.1021/acs.est.7b00397, 2017.

Canagaratna, M. R., Jayne, J. T., Jimenez, J. L., Allan, J. D., Alfarra, M. R., Zhang, Q., Onasch, T. B., Drewnick, F., Coe, H., Middlebrook, A., Delia, A., Williams, L. R., Trimborn, A. M., Northway, M. J., DeCarlo, P. F., Kolb, C. E., Davidovits, P., and Worsnop, D. R.: Chemical and microphysical characterization of ambient aerosols with the aerodyne aerosol mass spectrometer, Mass Spectrom. Rev., 26, 185–222, https://dx.doi.org/10.1002/mas.20115, 2007.

Chan, C. Y., Wong, K. H., Li, Y. S., Chan, Y., and Zhang, X.D.: The effects of Southeast Asia fire activities on tropospheric ozone, trace gases and aerosols at a remote site over the Tibetan Plateau of Southwest China, Tellus B, 58B, 310–318, https://doi.org/10.1111/j.1600-0889.2006.00187.x, 2017.

Chen, Y., Cao, J. J., Huang, R. J., Yang, F. M., Wang, Q. Y., and Wang, Y. C.: Characterization, mixing state, and evolution of urban single particles in Xi'an (China) during wintertime haze days, Sci. Total Environ., 573, 937–945, https://doi.org/10.1016/j.scitotenv.2016.08.151, 2016.

Chen, Y., Wenger, J. C., Yang, F. M., Cao, J. J., Huang, R. J., Shi, G. M., Zhang, S. M., Tian, M., and Wang, H. B.: Source characterization of urban particles from meat smoking activities in Chongqing, China using single particle aerosol mass spectrometry, Environ. Pollut., 228, 92–101, https://doi.org/10.1016/j.envpol.2017.05.022, 2017.

Chen, Y., Tian, M., Huang, R. J., Shi, G. M., Wang, H. B., Peng, C., Cao, J. J., Wang, Q. Y., Zhang, S. M., Guo, D. M., Zhang, L. M., and Yang, F. M.: Characterization of urban amine-containing particles in southwestern China: seasonal variation, source, and processing, Atmos. Chem. Phys., 19, 3245–3255, https://doi.org/10.5194/acp-19-3245-2019, 2019.

Chen, J. Q., and Bordoni, S.: Orographic effects of the Tibetan Plateau on the East Asian Summer Monsoon: An energetic perspective, J. Climate., 27, 3052–3072, https://doi.org/10.1175/JCLI-D-13-00479.1, 2014.

Cheng, C. L., Li, M., Chan, C. K., Tong, H. J., Chen, C. H., Chen, D. H., Wu, D., Li, L., Wu, C., Cheng, P., Gao, W., Huang, Z. X., Li, X., Zhang, Z. J., Fu, Z., Bi, Y. R., Zhou, Z.: Mixing state of acid containing particles in the rural area of Pearl River Delta, China: implicatio the formation mechanism of oxalic acid, Atmos. Chem. Phys., 17, 9519–9533, https://doi.org/10.5194/acp-17-9519-2017, 2017.

Crippa, M., DeCarlo, P. F., Slowik, J. G., Mohr, C., Heringa, M. F., Chirico, R., Poulain, L., Freutel, F., Sciare, J., Cozic, J., Di Marco, C. F., Elsasser, M., Nicolas, J. B., Marchand, N., Abidi, E., Wiedensohler, A., Drewnick, F., Schneider, J., Borrmann, S., Nemitz, E., Zimmermann, R., Jaffrezo, J. L., Prévôt, A. S. H., and Baltensperger, U.: Wintertime aerosol chemical composition and source apportionment of the organic fraction in the metropolitan area of Paris, Atmos. Chem. Phys., 13, 961–981, https://doi.org/10.5194/acp-13-961-2013, 2013.

Dall'Osto, M., Beddows, D.C.S., Gietl, J. K., Olatunbosun, O. A., Yang, X. G., and Harrison, R. M.: Characteristics of tyre dust in polluted air: studies by single particle mass spectrometry (ATOFMS), Atmos. Environ. 94, 224–230, https://doi.org/10.1016/j.atmosenv.2014.05.026, 2014.

Dall'Osto, M., and Harrison, R. M.: Urban organic aerosols measured by single particle mass spectrometry in the megacity of London, Atmos. Chem. Phys., 12, 4127–4142, http://dx.doi.org/10.5194/acp-12-4127–2012, 2012.

Ding, J., Dai, Q. L., Zhang, Y. F., Xu, J., Huangfu, Y. Q., Feng, Y. C.: Air humidity affects secondary aerosol formation in different pathways, Sci. Total Environ., 759, 143540–143549, https://doi.org/10.1016/j.scitotenv.2020.143540, 2021.

Draxler, R. and Hess, G.: An overview of the HYSPLIT_4 modelling system for trajectories, Aust.

550   Meteorol. Mag., 47, 295–308, 1998.

551 Du, W., Sun, Y. L., Xu, Y. S., Jiang, Q., Wang, Q. Q., Wang, W., Wang, F., Bai, Z. P., Zhao, X. D., and

552   Yang, Y. C.: Chemical characterization of submicron aerosol and particle growth events at a national

553   background site (3295 m a.s.l.) on the Tibetan Plateau, Atmos. Chem. Phys., 15, 10811–10824,

554   https://doi.org/10.5194/acp-15-10811-2015, 2015.

555 Engling, G., Zhang, Y. N., Chan, C. Y., Sang, X. F., Lin, M., Ho, K. F., Li, Y. S., Lin, C. Y., and Lee, J. J.:

556   Characterization and sources of aerosol particles over the southeastern Ti-betan Plateau during the

557   Southeast Asia biomass-burning season, Tellus B, 63, 117–128,

558   https://doi.org/10.1111/j.1600-0889.2010.00512.x, 2011.

559 Ervens, B., Turpin, B. J., and Weber, R. J.: Secondary organic aerosol formation in cloud droplets and

560   aqueous particles (aqSOA): a review of laboratory, feld and model studies, Atmos. Chem. Phys., 11,

561   11069–11102, https://doi.org/10.5194/acp-11-11069-2011, 2011.

562 Fang, X. Z., Liu, Y. Y., Li, K. J., Wang, T., Deng, Y., Feng, Y. Q., Yang, Y., Cheng, H. Y., Chen, J. M., and

563   Zhang, L. W.: Atmospheric Nitrate Formation through Oxidation by Carbonate Radical, ACS Earth

564   Space Chem., 5, 1801–1811, https://doi.org/10.1021/acsearthspacechem.1c00169, 2021.

565 Fry, J. L., Draper, D. C., Barsanti, K. C., Smith, J. N., Ortega, J., Winkler, P. M., Lawler, M. J., Brown, S.

566   S., Edwards, P. M., Cohen, R. C., and Lee, L.: Secondary Organic Aerosol Formation and Organic

567   Nitrate Yield from NO_3 Oxidation of Biogenic Hydrocarbons, Environ. Sci. Technol., 48,

568   11944–11953, https://doi.org/10.1021/es502204x, 2014.

569 Furukawa, T., and Takahashi, Y.: Oxalate metal complexes in aerosol particles: implications for the

570   hygroscopicity of oxalate-containing particles. Atmos. Chem. Phys., 11, 4289－4301,

571   https://doi.org10.5194/acp-11-4289-2011, 2011.

572 Gettelman, A., Morrison, H., Terai, C. R., and Wood, R.: Microphysical process rates and global

573   aerosolecloud interactions, Atmos. Chem. Phys., 13, 9855–9867,

574   https://doi.org/10.5194/acp-14-9099-2014, 2013.

575 Han, H., Wu, Y., Liu, J., Zhao, T. L., Zhuang, B. L., Wang, H. L., Li, Y. C., Chen, H. M., Zhu, Y., Liu, H.

576   N., Wang, Q. G., Li, S., Wang, T. J., Xie, M., and Li, M. M.: Impacts of atmospheric transport and

577   biomass burning on the inter-annual variation in black carbon aerosols over the Tibetan Plateau,

578   Atmos. Chem. Phys., 20, 13591–13610, https://doi.org/10.5194/acp-20-13591-2020, 2020.

579 Healy, R. M., Sciare, J., Poulain, L., Crippa, M., Wiedensohler, A., Prévôt, A.S.H., Baltensperger, U.,

580   Sarda-Estève, R., McGuire, M. L., Jeong, C. H., McGillicuddy, E., O'Connor, I. P., Sodeau, J. R.,

581   Evans, G. J., and Wenger, J. C.: Quantitative determination of carbonaceous particle mixing state in

582   Paris using single-particle mass spectrometer and aerosol mass spectrometer measurements, Atmos.

583   Chem. Phys., 13, 9479–9496, http://dx.doi.org/10.5194/acp-13-9479-2013, 2013.

584 Hua, S., Liu, Y. Z., Luo, R., Shao, T. B., Zhu, Q. Z.: Inconsistent aerosol indirect effects on water clouds

585   and ice clouds over the Tibetan Plateau, Int. J. Climatol., 40, 3832–3848,

586   https://doi.org/10.1002/joc.6430, 2019.

587 Huang, X. J., Zhang, J. K., Luo, B., Luo, J. Q., Zhang, W., and Rao, Z. H.: Characterization of oxalic

588   acid-containing particles in summer and winter seasons in Chengdu. China, Atmos. Environ., 198,

589   133–141. https://doi.org/10.1016/j.atmosenv.2018.10.050, 2019.

590 Immerzeel, W. W., van Beek, L. P. H., and Bierkens, M. F. P.: Climate change will affect the Asian water

591   towers, Science, 328, 1382–1385, https://doi.org/10.1126/science.1183188, 2010.

592 Jacobson, M. Z.: Analysis of aerosol interactions with numerical techniques for solving coagulation,

593   nucleation, condensation, dissolution, and reversible chemistry among multiple size distributions, J.

Geophys. Res., 107(D19), 4366, https://doi.org/10.1029/2001JD002044, 2002.

Jiang, H. H., Frie, A. L., Lavi, A., Chen, J. Y., Zhang, H., Bahreini, R., and Lin, Y. H.: Brown carbon formation from nighttime chemistry of unsaturated heterocyclic volatile organic compounds, Environ. Sci. Technol. Lett., 6, 184190, https://doi.org/10.1021/acs.estlett.9b00017, 2019.

Kumar, M., Raju, M. P., Singh, R. K., Singh, A. K., Singh, R. S., and Banerjee, T.: Wintertime characteristics of aerosols over middle Indo-Gangetic Plain: vertical profile, transport and radiative forcing, Atmos. Res., 183, 268–282, https://doi.org/10.1016/j.atmosres.2016.09.012, 2017.

Kundu, S., Kawamura, K., Andreae, T. W., Hoffer, A., and Andreae, M. O.: Molecular distributions of dicarboxylic acids, ketocarboxylic acids and alpha-dicarbonyls in biomass burning aerosols: implications for photochemical production and degradation in smoke layers, Atmos. Chem. Phys., 10 (5), 2209−2225, https://doi.org/10.5194/acp-10-2209-2010, 2010.

Lian, X. F., Zhang, G. H., Yang, Y. X., Lin, Q. H., Fu, Y. Z., Jiang, F., Peng, L., Hu, X. D., Chen, D. H., Wang, X. M., Peng, P. A., Sheng, G. Y., and Bi, X. H.: Evidence for the Formation of Imidazole from Carbonyls and Reduced Nitrogen Species at the Individual Particle Level in the Ambient Atmosphere, Environ. Sci. Technol. Lett., 8, 9–15. https://dx.doi.org/10.1021/acs.estlett.0c00722, 2021.

Liang, Z. C., Zhou, L. Y., Cuevas, R. A., Li, X. Y., Cheng,C. L., Li, M., Tang, R. Z., Zhang, R. F., Lee Patrick K. H., Lai, Alvin C. K., and Chan, C.K.: Sulfate Formation in Incense Burning Particles: A Single-Particle Mass Spectrometric Study, Environ. Sci. Technol. Lett., 9, 718–725, https://doi.org/10.1021/acs.estlett.2c00492, 2022.

Li, C. L., Bosch, C., Kang, S. C., Andersson, A., Chen, P. F., Zhang, Q. G., Cong, Z. Y., Chen, B., Qin, D. H., and Gustafsson., Ö.: Sources of black carbon to the Himalayan–Tibetan Plateau glaciers, Nat. Commun., 7, 12574, https://doi.org/10.1038/ncomms12574, 2016b.

Li, C. L., Bosch, C., Kang, S. C., Andersson, A., Chen, P. F., Zhang, Q. G., Cong, Z. Y., Tripathee, L., and Örjanb, G.: ^{14}C characteristics of organic carbon in the atmosphere and at glacier region of the Tibetan Plateau, Sci. Total Environ., 832, 155020, https://doi.org/10.1016/j.scitotenv.2022.155020, 2022a.

Li, L., Huang, Z. X., Dong, J. G., Li, M., Gao, W., Nian, H. Q., Fu, Z., Zhang, G. H., Bi, X. H., Cheng, P., and Zhou, Z.: Real time bipolar time-of-flight mass spectrometer for analyzing single aerosol particles, Int. J. Mass Spectrom., 303, 118–124, https://doi.org/10.1016/j.ijms.2011.01.017, 2011.

Li L., Wang, Q. Y., Zhang, Y., Liu, S. X., Zhang, T., Wang, S., Tian, J., Chen, Y., Hang Ho, S. S., Han, Y., and Cao, J.J.: Impact of reduced anthropogenic emissions on chemical characteristics of urban aerosol by individual particle analysis, Chemosphere, 303, 135013, https://doi.org/10.1016/j.chemosphere.2022.135013, 2022b.

Li, J. J., Wang, G. H., Wang, X. M., Cao, J. J., Sun, T., Cheng, C. L., Meng, J. J., Hu, T. F., and Liu, S. X.: Abundance, composition and source of atmospheric $PM_{2.5}$ at a remote site in the Tibetan Plateau, China, Tellus B, 65, http://dx.doi.org/10.3402/tellusb.v65i0.20281, 2013.

Li, Y. J., Sun, Y. L., Zhang, Q., Li, X., Li, M., Zhou, Z., and Chan, C. K.: Real-time chemical characterization of atmospheric particulate matter in China: A review, Atmos. Environ., 158, 270–304, http://dx.doi.org/10.1016/j.atmosenv.2017.02.027, 2017.

Lin, Q. H., Bi, X. H., Zhang, G. H., Yang, Y. X., Peng, L., Lian, X. F., Fu, Y. Z., Li, M., Chen, D. H., Miller, M., Ou, J., Tang, M. J., Wang, X. M., Peng, P. A., Sheng, G. Y., and Zhou, Z.: In-cloud formation of secondary species in iron-containing particles, Atmos. Chem. Phys., 19, 1195–1206, https://doi.org/10.5194/acp-19-1195-2019, 2019

Link, M. F., Kim, J., Park, G., Lee, T., Park, T., Babar, Z. B., Sung, K., Kim, P., Kang, S., Kim, J. S., Choi, Y., Son, J., Lim, H. J., and Farmer, D.K.: Elevated production of NH_4NO_3 from the photochemical

638   processing of vehicle exhaust: Implications for air quality in the Seoul Metropolitan Region, Atmos.
639   Environ., 156, 95–101, https://doi.org/10.1016/j.atmosenv.2017.02.031, 2017.

640   Liu, Y. Z., Zhu, Q. Z., Huang, J. P., Hua, S., and Jia, R.: Impact of dust-polluted convective clouds over the
641   Tibetan Plateau on downstream precipitation, Atmos. Environ., 209, 67–77,
642   https://doi.org/10.1016/j.atmosenv.2019.04.001, 2019.

643   Liu, Q., Liu, D. T., Gao, Q., Tian, P., Wang, F., Zhao, D. L., Bi, K., Wu, Y. Z., Ding, S., Hu, K., Zhang, J.
644   L., Ding, D. P., and Zhao, C. S.: Vertical characteristics of aerosol hygroscopicity and impacts on
645   optical properties over the North China Plain during winter, Atmos. Chem. Phys., 20, 3931–3944,
646   https://doi.org/10.5194/acp-20-3931-2020, 2020a.

647   Liu, D. T., Hu, K., Zhao, D. L., Ding, S., Wu, Y. F., Zhou, C., Yu, C. J., Tian, P., Liu, Q., Bi, K., Wu, Y. Z.,
648   Hu, B., Ji, D. S., Kong, S. F., Ouyang, B., He, H., Huang, M. Y., and Ding, D.P.: Efficient Vertical
649   Transport of Black Carbon in the Planetary Boundary Layer, Geo. Res. Lett., 47, 1–10, https://doi.org/
650   10.1029/2020GL088858, 2020b

651   Liu, H. K., Wang, Q. Y., Xing, L., Zhang, Y., Zhang, T., Ran, W. K., and Cao, J. J.: Measurement report:
652   quantifying source contribution of fossil fuels and biomass-burning black carbon aerosol in the
653   southeastern margin of the Tibetan Plateau, Atmos. Chem. Phys., 21, 973–987,
654   https://doi.org/10.5194/acp-21-973-2021, 2021.

655   Liu, X. D., Dong, B. W., Yin, Z. Y., Smith, R. S., Guo, Q. C.: Continental drift and plateau uplift control
656   origination and evolution of Asian and Australian monsoons, Sci. Rep., 7, 40344, https://doi.org/
657   10.1038/srep40344, 2017.

658   Luo, M., Liu, Y. Z., Zhu, Q. Z., Tang, Y. H., and Alam, K.: Role and mechanisms of black carbon affecting
659   water vapor transport to Tibet, Remote Sens., 12, 231, https://doi.org/10.3390/rs12020231, 2020.

660   Ma, L., Li, M., Huang, Z. X., Li, L., Gao, W., Nian, H. Q., Zou, L. L., Fu, Z., Gao, J., Chai, F. H., and
661   Zhou, Z.: Real time analysis of lead-containing atmospheric particles in Beijing during springtime by
662   single particle aerosol mass spectrometry, Chemosphere, 154, 454–462,
663   https://doi.org/10.1016/j.chemosphere.2016.04.001, 2016.

664   Ma, X., Yu, F., and Luo, G.: Aerosol direct radiative forcing based on GEOS-Chem-APM and uncertainties,
665   Atmos. Chem. Phys., 12, 5563–5581, https://doi.org/10.5194/acp-12-5563-2012, 2012.

666   Matsui, H.: Black carbon simulations using a size- and mixingstate-resolved three-dimensional model: 2.
667   Aging timescale and its impact over East Asia, J. Geophys. Res.-Atmos., 121, 1808–1821,
668   https://doi.org/10.1002/2015jd023999, 2016.

669   Meng, J. J, Wang, G. H, Li, J. J, Cheng, C. L, Ren, Y. Q, Huang, Y., Cheng, Y. T, Cao, J. J, and Zhang, T.:
670   Seasonal characteristics of oxalic acid and related SOA in the free troposphere of Mt. Hua, central
671   China: implications for sources and formation mechanisms, Sci. Total Environ., 493, 1088–1097,
672   https://doi.org/10.1016/j.scitotenv.2014.04.086, 2014.

673   Meng, J. J., Liu, X. D., Hou, Z. F., Yi, Y. N., Yan, L., Li, Z., Cao, J.J., Li, J. J., Wang, G. H.: Molecular
674   characteristics and stable carbon isotope compositions of dicarboxylic acids and related compounds in
675   the urban atmosphere of the North China Plain: implications for aqueous phase formation of SOA
676   during the haze periods, Sci. Total Environ., 705, 135256,
677   https://doi.org/10.1016/j.scitotenv.2019.135256, 2020.

678   Ng, N. L., Canagaratna, M. R., Jimenez, J. L., Chhabra, P. S., Seinfeld, J. H., and Worsnop, D. R.: Changes
679   in organic aerosol composition with aging inferred from aerosol mass spectra, Atmos. Chem. Phys.,
680   11(13), 6465-6474, https://doi.org/10.5194/acp-11-6465-2011, 2011.

681   Peng, J. F., Hu, M., Guo, S., Du, Z. F., Zheng, J., Shang, D. J., Zamora, M. L., Zeng, L. M., Shao, M., Wu,

682   Y. S., Zheng, J., Wang, Y., Glen, C. R., Collins, D. R., Molina, M. J., and Zhang, R. Y.: Markedly
683   enhanced absorption and direct radiative forcing of black carbon under polluted urban environments,
684   P. Natl. Acad. Sci. USA, 113, 4266–4271, https://doi.org/10.1073/pnas.1602310113, 2016.

685   Pratt, K. A., Hatch, L. E., and Prather, K. A.: Seasonal volatility dependence of ambient particle phase
686   amines, Environ. Sci. Technol., 43, 5276–5281, https://doi.org/10.1021/es803189n, 2009.

687   Pratt, K. A., Murphy, S. M., Subramanian, R., DeMott, P. J., Kok, G. L., Campos, T., Rogers, D. C., Prenni,
688   A. J., Heymsfield, A. J., Seinfeld, J. H., and Prather, K. A.: Flight-based chemical characterization of
689   biomass burning aerosols within two prescribed burn smoke plumes, Atmos. Chem. Phys., 11,
690   12549–12565, https://doi.org/10.5194/acp-11-12549-2011, 2011.

691   Qian, Y., Flanner, M. G., Leung, L. R., and Wang, W.: Sensitivity studies on the impacts of Tibetan Plateau
692   snowpack pollution on the Asian hydrological cycle and monsoon climate, Atmos. Chem. Phys., 11,
693   1929-1948, https://doi.org/10.5194/acp-11-1929-2011, 2011.

694   Rehbein, P. J., Jeong, C. H., McGuire, M. L., Yao, X., Corbin, J. C., and Evans, G. J.: Cloud and fog
695   processing enhanced gas-toparticle partitioning of trimethylamine, Environ. Sci. Technol., 45,
696   4346–4352, https://doi.org/10.1021/es1042113, 2011.

697   Roth, A., Schneider, J., Klimach, T., Mertes, S., van Pinxteren, D., Herrmann, H., and Borrmann, S.:
698   Aerosol properties, source identification, and cloud processing in orographic clouds measured by
699   single particle mass spectrometry on a central European mountain site during HCCT-2010, Atmos.
700   Chem. Phys., 16, 505–524, https://doi.org/10.5194/acp-16-505-2016, 2016.

701   Shen, L. J., Wang, H. L., Yin, Y., Chen, J. H., and Chen, K.: Observation of atmospheric new particle
702   growth events at the summit of mountain Tai (1534 m) in Central East China, Atmos. Environ., 201,
703   148–157, https://doi.org/10.1016/j.atmosenv.2018.12.051, 2019.

704   Shen, L. J., Wang, H. L., Lü, S., Zhang, X. H., Yuan, J., Tao, S. K., Zhang, G. J., Wang, F., and Li, L.:
705   Influence of pollution control on air pollutants and the mixing state of aerosol particles during the 2nd
706   World Internet Conference in Jiaxing, China, J. Clean. Prod., 149, 436–447,
707   https://doi.org/10.1016/j.jclepro.2017.02.114, 2017.

708   Shen, R. Q., Ding, X., He, Q. F., Cong, Z. Y., Yu, Q. Q., and Wang, X. M.: Seasonal variation of secondary
709   organic aerosol tracers in Central Tibetan Plateau, Atmos. Chem. Phys., 15, 8781-8793,
710   https://doi.org/10.5194/acp-15-8781-2015, 2015.

711   Sirois, A. and Bottenheim, J. W.: Use of backward trajectories to interpret the 5-year record of PAN and O_3
712   ambient air concentrations at Kejimkujik National Park, Nova Scotia, J. Geophys. Res., 100,
713   2867–2881, https://doi.org/10.1029/94JD02951, 1995.

714   Song, X. H., and Hopke, P. K.: Classifcation of single particles analyzed by ATOFMS using an artifcial
715   neural network, ART-2A, Anal. Chem., 71, 860–865, https://doi.org/10.1021/ac9809682, 1999.

716   Sorooshian, A., Lu, M. L., Brechtel, F. J., Jonsson, H., Feingold, G., Flagan, R. C., and Seinfeld, J. H.: On
717   the source of organic acid aerosol layers above clouds, Environ. Sci. Technol., 41, 4647–4654,
718   https://doi.org/10.1021/es0630442, 2007.

719   Sullivan, R. C., Guazzotti, S. A., Sodeman, D. A., and Prather, K. A.: Direct observations of the
720   atmospheric processing of Asian mineral dust, Atmos. Chem. Phys., 7, 1213–1236,
721   https://doi.org/10.5194/acp-7-1213-2007, 2007.

722   Sun, Y. L, Wang, Z. F., Fu, P. Q., Jiang, Q. J., Yang, T., Li, J., and Ge, X. L.: The impact of relative
723   humidity on aerosol composition and evolution processes during wintertime in Beijing, China, Atmos.
724   Environ., 77, 927–934, https://doi.org/10.1016/j.atmosenv.2013.06.019, 2013.

725   Tian, J., Wang, Q. Y., Zhang, Y., Yan, M. Y., Liu, H. K., Zhang, N. N., Ran, W. K., and Cao, J. J.: Impacts

726   of primary emissions and secondary aerosol formation on air pollution in an urban area of China
727   during   the   COVID-19   lockdown,   Environ.   Int.,   150,   106426–14,
728   https://doi.org/10.1016/j.envint.2021.106426, 2021.
729 Wang, A. Q., Xie, X. N., Liu, X. D., and Yin, Z. Y.: Direct Radiative Effect (DRE) of Dust Aerosols on
730   West African and East Asian Monsoon: The Role of Ocean-Atmosphere Interactions, J. Geophys.
731   Res.Atmos., 127, 1–20, https://doi.org/10.1029/2021JD035917, 2022.
732 Wang, G. H., Zhang, R. Y., Gomez, M. E., Yang, L. X., Zamora, M. L., Hu, M., Lin, Y., Peng, J. F., Guo, S.,
733   Meng, J. J., Li, J. J., Cheng, C. L., Hu, T. F., Ren, Y. Q., Wang, Y. S., Gao, J., Cao, J. J., An, Z. S.,
734   Zhou, W. J., Li, G. H., Wang, J. Y., Tian, P. F., Marrero-Ortiz, W., Secrest, J., Du, Z. F., Zheng, J.,
735   Shang, D. J., Zeng, L. M., Shao, M., Wang, W. G., Huang, Y., Wang, Y., Zhu, Y. J., Li, Y. X., Hu, J. X.,
736   Pan, B. W., Cai, L., Cheng, Y. T., Ji, Y. M., Zhang, Y., Rosenfeld, D., Liss, P. S., Duce, R. A., Kolb, C.
737   E., and Molina., M. J.: Persistent sulfate formation from London Fog to Chinese haze, P. Natl. Acad.
738   Sci. USA, 113(48), 13630–13635, https://doi.org/10.1073/pnas.1616540113, 2016.
739 Wang, H. C., Lu, K. D., Chen, X. R., Zhu, Q. D., Chen, Q., Guo, S., Jiang, M. Q., Li, X., Shang, D. J., Tan,
740   Z. F., Wu, Y. S., Wu, Z. J., Zou, Q., Zheng, Y., Zeng, L. M., Zhu, T., Hu, M., Zhang, Y. H.: High
741   N2O5 concentrations observed in urban Beijing: implications of a large nitrate formation pathway,
742   Environ. Sci. Technol. Lett., 4, 416–420, https://doi.org/10.1021/acs.estlett.7b00341, 2017.
743 Wang, H. L., An, J. L., Shen, L. J., Zhu, B., Xia, L., Duan, Q., and Zou, J. N.: Mixing state of ambient
744   aerosols in Nanjing city by single particle mass spectrometry, Atmos. Environ., 132, 123–132,
745   https://dx.doi.org/10.1016/j.atmosenv.2016.02.032, 2016.
746 Wang, Q. Y., Han, Y. M., Ye, J. H., Liu, S. X., Pongpiachan, S., Zhang, N. N., Han, Y. M., Tian, J., Wu, C.,
747   Long, X., Zhang, Q., Zhang, W. Y., Zhao, Z. Z., and Cao, J. J.: High contribution of secondary brown
748   carbon to aerosol light absorption in the southeastern margin of Tibetan Plateau, Geophys. Res. Lett.,
749   46, 4962–4970, https://doi.org/10.1029/2019GL082731, 2019a.
750 Wang, H. L., Shen, L. J., Yin, Y., Chen, K., Chen, J. H., and Wang, Y. S.: Characteristics and mixing state
751   of aerosol at the summit of Mount Tai (1534 m) in Central East China: First measurements with
752   SPAMS, Atmos. Environ., 213, 273–284, https://doi.org/10.1016/j.atmosenv.2019.06.021, 2019b.
753 Wang, Q. Y., Cao, J. J., Han, Y. M., Tian, J., Zhu, C. S., Zhang, Y., Zhang, N. N., Shen, Z. X., Ni, H. Y.,
754   Zhao, S. Y., and Wu, J. R.: Sources and physicochemical characteristics of black carbon aerosol from
755   the southeastern Tibetan Plateau: internal mixing enhances light absorption, Atmos. Chem. Phys., 18,
756   4639–4656, https://doi.org/10.5194/acp-18-4639-2018, 2018.
757 Wenzel, R. J., Liu, D.-Y., Edgerton, E. S., and Prather, K. A.: Aerosol time-of-flight mass spectrometry
758   during the Atlanta Supersite Experiment: 2. Scaling procedures, J. Geophys. Res., 108, 8427,
759   http://dx.doi.org/10.1029/2001jd001563, 2003.
760 Wood, E. C., Canagaratna, M. R., Herndon, S. C., Onasch, T. B., Kolb, C. E., Worsnop, D. R., Kroll, J. H.,
761   Knighton, W. B., Seila, R., Zavala, M., Molina, L. T., DeCarlo, P. F., Jimenez, J. L., Weinheimer, A. J.,
762   Knapp, D. J., Jobson, B. T., Stutz, J., Kuster, W. C., and Williams, E. J.: Investigation of the
763   correlation between odd oxygen and secondary organic aerosol in Mexico City and Houston, Atmos.
764   Chem. Phys., 10, 8947–8968, https://doi.org/10.5194/acp-10-8947-2010, 2010.
765 Xu, L. L., Wu, X., Hong, Z. Y., Zhang, Y. R., Deng, J. J., Hong, Y. W., and Chen, J. S.: Composition,
766   mixing state, and size distribution of single submicron particles during pollution episodes in a coastal
767   city   in   southeast   China,   Environ.   Sci.   Pollut.   Res.,   26,   1464–1473,
768   https://doi.org/10.1007/s11356-018-3469-x, 2018.
769 Xu, W. Q., Han, T. T., Du, W., Wang, Q. Q., Chen, C., Zhao, J., Zhang, Y. J., Li, J., Fu, P. Q., Wang, Z. F.,

Worsnop, D. R., and Sun, Y. L.: Effects of aqueous-phase and photochemical processing on secondary organic aerosol formation and evolution in Beijing, China, Environ. Sci. Technol., 51, 762−770, https://doi.org/10.1021/acs.est.6b04498, 2017.

Xue, J., Griffth, S. M., Yu, X., Lau, A.K.H., and Yu, J. Z.: Effect of nitrate and sulfate relative abundance in $PM_{2.5}$ on liquid water content explored through half-hourly observations of inorganic soluble aerosols at a polluted receptor site, Atmos. Environ., 99, 24–31, https://doi.org/10.1016/j.atmosenv.2014.09.049, 2014.

Yang, J., Ma, S. X., Gao, B., Li, X. Y., Zhang, Y. J., Cai, J., Li, M., Yao, L. A., Huang, B., and Zheng, M.: Single particle mass spectral signatures from vehicle exhaust particles and the source apportionment of on-line $PM_{2.5}$ by single particle aerosol mass spectrometry, Sci. Total Environ., 593, 310–318, https://doi.org/10.1016/j.scitotenv.2017.03.099, 2017.

Zauscher, M. D., Wang, Y., Moore, M. J. K., Gaston, C. J., and Prather, K. A.: Air Quality Impact and Physicochemical Aging of Biomass Burning Aerosols during the 2007 San Diego Wildfires, Environ. Sci. Technol., 47, 7633–7643, https://doi.org/10.1021/es4004137, 2013.

Zaveri, R. A., Barnard, J., Easter, R., Riemer, N., and West, M.: Particle-resolved simulation of aerosol size, composition, mixing state, and the associated optical and cloud condensation nuclei activation properties in an evolving urban plume, J. Geophys. Res., 115, D17210, https://doi.org/10.1029/2009JD013616, 2010.

Zhang, G. H., Bi, X. H., Chan, L. Y., Li, L., Wang, X. M., Feng, J. L., Sheng, G. Y., Fu, J. M., Li, M., and Zhou, Z.: Enhanced trimethylamine-containing particles during fog events detected by single particle aerosol mass spectrometry in urban Guangzhou, China, Atmos. Environ., 55, 121–126, https://doi.org/10.1016/j.atmosenv.2012.03.038, 2012.

Zhang, G. H., Han, B. X., Bi, X. H., Dai, S. X., Huang, W., Chen, D. H., Wang, X. M., Sheng, G. Y., Fu, J. M., and Zhou, Z.: Characteristics of individual particles in the atmosphere of Guangzhou by single particle mass spectrometry, Atmos. Res., 153, 286–295, https://doi.org/10.1016/j.atmosres.2014.08.016, 2015.

Zhang, J. K., Luo, B., Zhang, J. Q., Ouyang, F., Song, H. Y., Liu, P. C., Cao, P., Schäfer, K., Wang, S. G., Huang, X. J., and Lin, Y. F.: Analysis of the characteristics of single atmospheric particles in Chengdu using single particle mass spectrometry, Atmos. Environ., 157, 91−100, https://doi.org/10.1016/j.atmosenv.2017.03.012, 2017a.

Zhang, G. H., Lin, Q. H., Peng, L., Yang, Y. X., Fu, Y. Z., Bi, X. H., Li, M., Chen, D. H., Chen, J. X., Cai, Z., Wang, X. M., Peng, P. A., Sheng, G. Y., Zhou, Z.: Insight into the in-cloud formation of oxalate based on in situ measurement by single particle mass spectrometry, Atmos. Chem. Phys., 17 (22), 13891–13901, https://doi.org/10.5194/acp-17-13891-2017, 2017b.

Zhang, G. H., Han, B. X., Bi, X. H., Dai, S. X., Huang, W., Chen, D. H., Wang, X. M., Sheng, G. Y., Fu, J. M., and Zhou, Z.: Characteristics of individual particles in the atmosphere of Guangzhou by single particle mass spectrometry, Atmos. Res., 153, 286–295, https://dx.doi.org/10.1016/j.atmosres.2014.08.016, 2015.

Zhang, G. H., Lian, X. F., Fu, Y. Z., Lin, Q. H., Li, L., Song, W., Wang, Z. Y., Tang, M. J., Chen, D. H., Bi, X. H., Wang, X. M., and Sheng, G. Y.: High secondary formation of nitrogen-containing organics (NOCs) and its possible link to oxidized organics and ammonium, Atmos. Chem. Phys., 20, 1469–1481, https://doi.org/10.5194/acp-20-1469-2020, 2020.

Zhang, X. H., Xu, J. Z., Kang, S. C., Zhang, Q., and Sun, J. Y.: Chemical characterization and sources of submicron aerosols in the northeastern Qinghai–Tibet Plateau: insights from high-resolution mass

25

spectrometry, Atmos. Chem. Phys., 19, 7897−7911, https://doi.org/10.5194/acp-19-7897-2019, 2019a.

Zhang, G. H., Lin, Q. H., Peng, L., Yang, Y. X., Jiang, F., Liu, F. X., Song, W., Chen, D. H., Cai, Z., Bi, X. H., Miller, M., Tang, M. J., Huang, W. L., Wang, X. M., Peng, P. A., Shen, G. Y.: Oxalate Formation Enhanced by Fe-Containing Particles and Environmental Implications, Environ. Sci. Technol., 53, 1269–1277, https://doi.org/10.1021/acs.est.8b05280, 2019b.

Zhang, N. N., Cao, J. J., Xu, H. M., and Zhu, C. S.: Elemental compositions of $PM_{2.5}$ and TSP in Lijiang, southeastern edge of Tibetan Plateau during pre-monsoon period, Particuology, 11(1), 63–69, https://doi.org/10.1016/j.partic.2012.08.002, 2013.

Zhang, S. P., Xing, J., Sarwar, G., Ge, Y. L., He, H., Duan, F. K., Zhao, Y., He, K. B., Zhu, L. D., Chu, B. W.: Parameterization of heterogeneous reaction of SO_2 to sulfate on dust with coexistence of NH_3 and NO_2 under different humidity conditions, Atmos. Environ., 208, 133–140, https://doi.org/10.1016/j.atmosenv.2019.04.004, 2019c.

Zhao, S. Y., Tie, X. X., Long, X., and Cao, J. J.: Impacts of Himalayas on black carbon over the Tibetan Plateau during summer monsoon, Sci. Total Environ., 598, 307–318, https://doi.org/10.1016/j.scitotenv.2017.04.101, 2017.

830 Table 1. The number concentrations, average percentages and characteristic ions of nine types
831 of particles during the entire study period, and the average percentages of the major six
832 particle types during two episodes.

Type	Number count	Fraction in total (%)	Episode 1 (%)	Episode 2 (%)	Tracer ions
rich-K	151040	30.9	29.0	39.3	$^{39}K^+$, $^{26}CN^-$, $^{42}CNO^-$, $^{46}NO_2^-$, $^{62}NO_3^-$, $^{97}HSO_4^-$
BB	91322	18.7	11.5	14.2	$^{39}K^+$, levoglucosan ($^{45}CHO_2^-$, $^{59}C_2H_3O_2^-$, $^{71}C_3H_3O_2^-$, $^{73}C_3HO_3^-$), $^{26}CN^-$, $^{35,37}Cl^-$, $^{42}CNO^-$, $^{46}NO_2^-$, $^{62}NO_3^-$, $^{97}HSO_4^-$
OC	62446	12.8	8.1	10.0	$^{27}C_2H_3^+$, $^{37}C_3H^+$, $^{38}C_3H_2^+$, $^{39}K^+/C_3H_3^+$, $^{43}C_2H_3O^+$, $^{51}C_4H_3^+$, $^{26}CN^-$, $^{42}CNO^-$, $^{46}NO_2^-$, $^{62}NO_3^-$, $^{97}HSO_4^-$
Ammonium	58317	11.9	17.5	13.5	$^{12}C^+$, $^{18}NH_4^+$, $^{39}K^+$, $^{58}C_2H_5NHCH_2^+$, $^{97}HSO_4^-$, $^{195}H(HSO_4)_2^-$
EC-aged	53337	10.9	10.0	17.2	$C_n^\pm$ (n =1 ~ 5), $^{39}K^+$, $^{97}HSO_4^-$
Dust	52533	10.7	20.3	1.3	$^{40}Ca^+$, $^{56}CaO^+$, $^{16}O^-$, $^{17}OH^-$, $^{76}SiO_3^-$, $^{79}PO_3^-$
NaK-SN	13726	2.8	na	na	$^{23}Na^+$, $^{39}K^+$, $^{62}NO_3^-$, $^{97}HSO_4^-$
Metal	4672	1.0	na	na	$^{51}V^+$, $^{56}Fe^+$, $^{64,66,68}Zn^+$, $^{206,207,208}Pb^+$
Others	1580	0.3	na	na	No obvious characteristic peaks

833

Figure captions:

Figure 1. Box and whisker diurnal plots of the number concentration of the main particle types (a) rich-Potassium (K), (b) Biomass burning (BB), (c) Organic carbon (OC), (d) Ammonium, (e) Element carbon (EC)-aged, (f) Dust in hourly resolution. The lower, middle, and upper lines of the boxes denote the 25th, 50th, and 75th percentiles. The lower and upper whiskers show the 10th and 90th percentiles, respectively. Average values are shown in white dots.

Figure 2. Maps of the mean HYSPLIT back trajectory clusters (72 h) at the height of 500 m during the whole field observation. Embedded pie chart represents the relative fraction of each particle type in the four clusters.

Figure 3. Size distributions of (a) the total number particle counts, (b) the relative percentages (%) of the total particles for nine groups during the sampling campaign.

Figure 4. Number fractions of secondary markers associated with the six particle types (rich-K, BB, OC, Ammonium, EC-aged, Dust). Secondary species include sulfate ($^{97}HSO_4^-$), sulfuric acid ($^{195}H(HSO_4)_2^-$), nitrate ($^{62}NO_3^-$), ammonium ($^{18}NH_4^+$), amine ($^{58}C_2H_5NHCH_2^+$), and oxalate ($^{89}HC_2O_4^-$) ions.

Figure 5. Number fractions of secondary markers associated with the six particle types (i.e., rich-K, BB, OC, Ammonium, EC-aged, and Dust) in four clusters. Secondary markers include sulfate ($^{97}HSO_4^-$), sulfuric acid ($^{195}H(HSO_4)_2^-$), nitrate ($^{62}NO_3^-$), ammonium ($^{18}NH_4^+$), amine ($^{58}C_2H_5NHCH_2^+$), and oxalate ($^{89}HC_2O_4^-$).
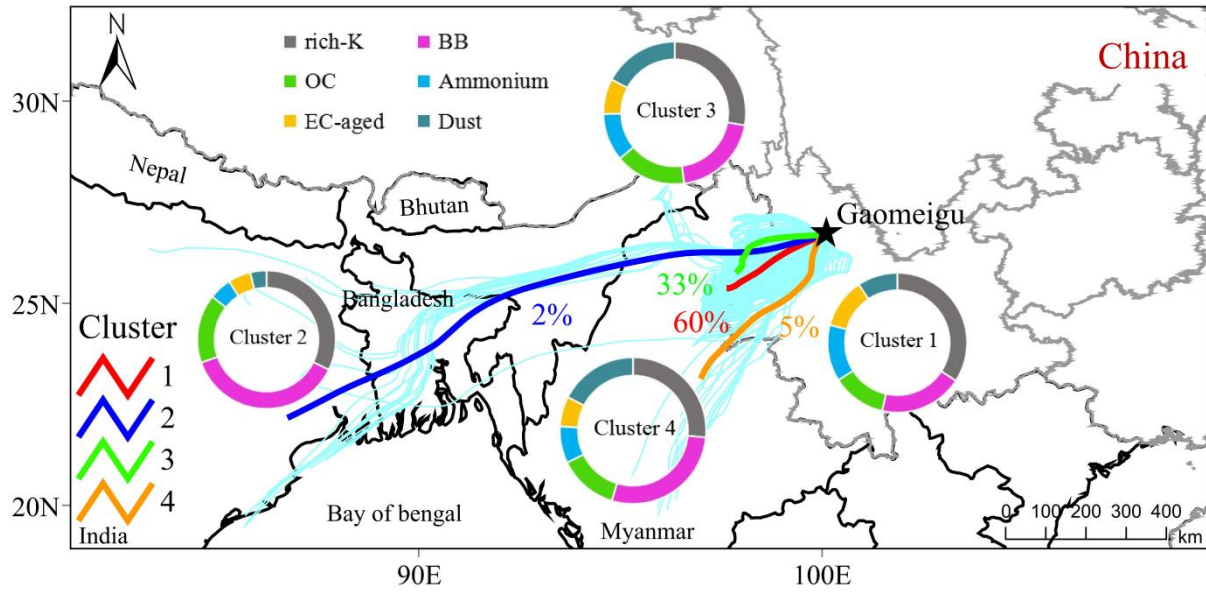
Figure 6. Correlations between the relative number fractions of the secondary species (a) $^{43}C_2H_3O^+$, (b) $^{89}HC_2O_4^-$, (c) $^{18}NH_4^+$, (d) $^{62}NO_3^-$, (e) $^{97}HSO_4^-$ and O_x concentration during E1 (blue square) and E2 (red dot).

Figure 7. Correlations between the relative number fractions of the secondary species (a) $^{43}C_2H_3O^+$, (b) $^{89}HC_2O_4^-$, (c) $^{18}NH_4^+$, (d) $^{62}NO_3^-$, (e) $^{97}HSO_4^-$ and relative humidity (RH) during E1 (cyan dot) and E2 (orange square).
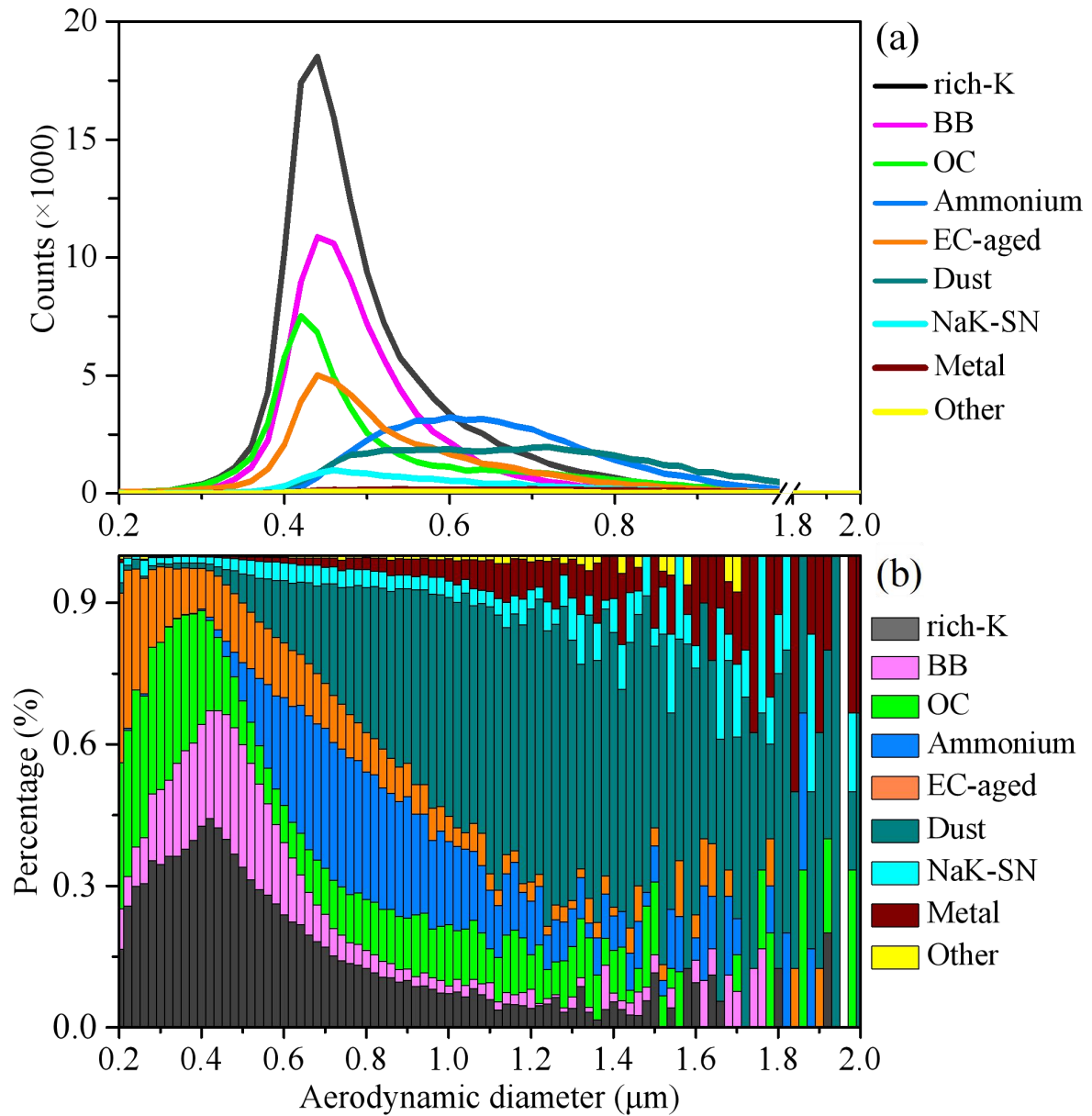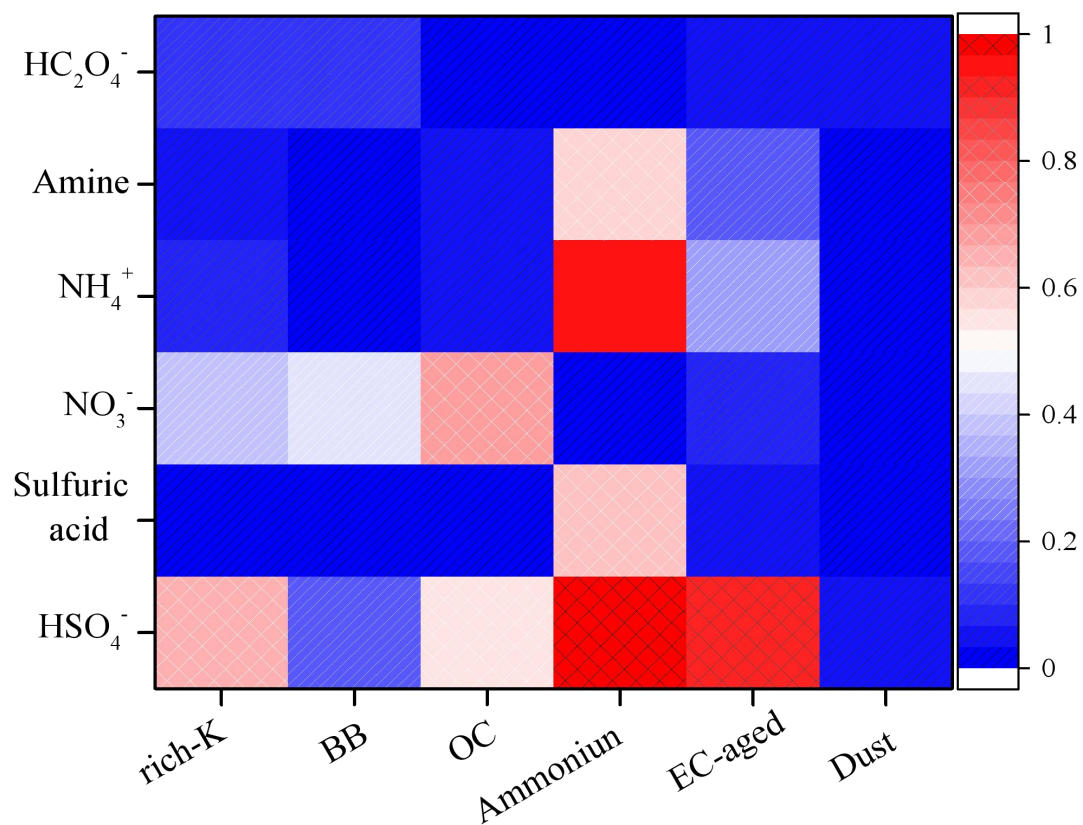
860

861 Figure 1. Box and whisker diurnal plots of the number concentration of the main particle types (a)

862 rich-Potassium (K), (b) Biomass burning (BB), (c) Organic carbon (OC), (d) Ammonium, (e) Element

863 carbon (EC)-aged, (f) Dust in hourly resolution. The lower, middle, and upper lines of the boxes denote the

864 25th, 50th, and 75th percentiles. The lower and upper whiskers show the 10th and 90th percentiles,

865 respectively. Average values are shown in white dots.

866

Figure 2. Maps of the mean HYSPLIT back trajectory clusters (72 h) at the height of 500 m during the whole field observation. Embedded pie chart represents the relative fraction of each particle type in the four clusters.

Figure 3. Size distributions of (a) the total number particle counts, (b) the relative percentages (%) of the total particles for nine groups during the sampling campaign.
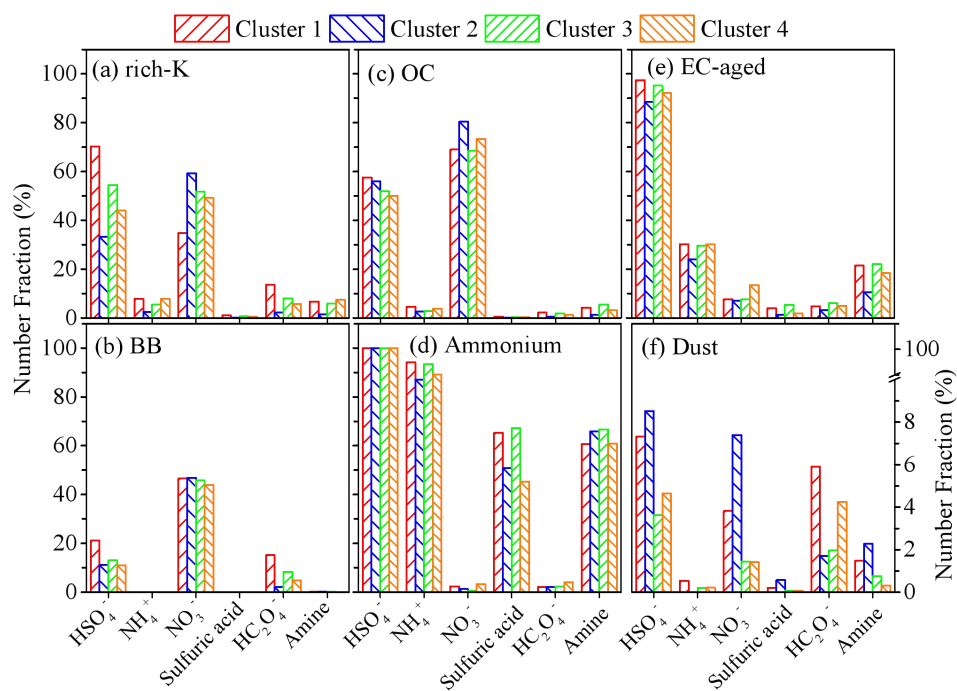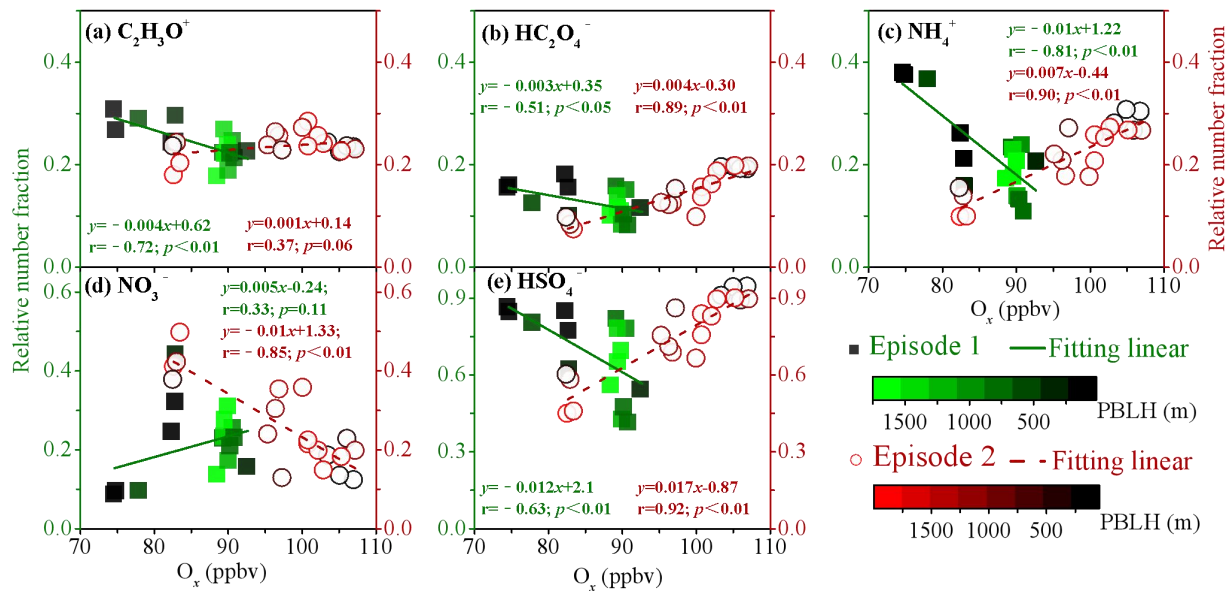
Figure 4. Number fractions of secondary markers associated with the six particle types (rich-K, BB, OC, Ammonium, EC-aged, Dust). Secondary species include sulfate ($^{97}HSO_4^-$), sulfuric acid ($^{195}H(HSO_4)_2^-$), nitrate ($^{62}NO_3^-$), ammonium ($^{18}NH_4^+$), amine ($^{58}C_2H_5NHCH_2^+$), and oxalate ($^{89}HC_2O_4^-$) ions.
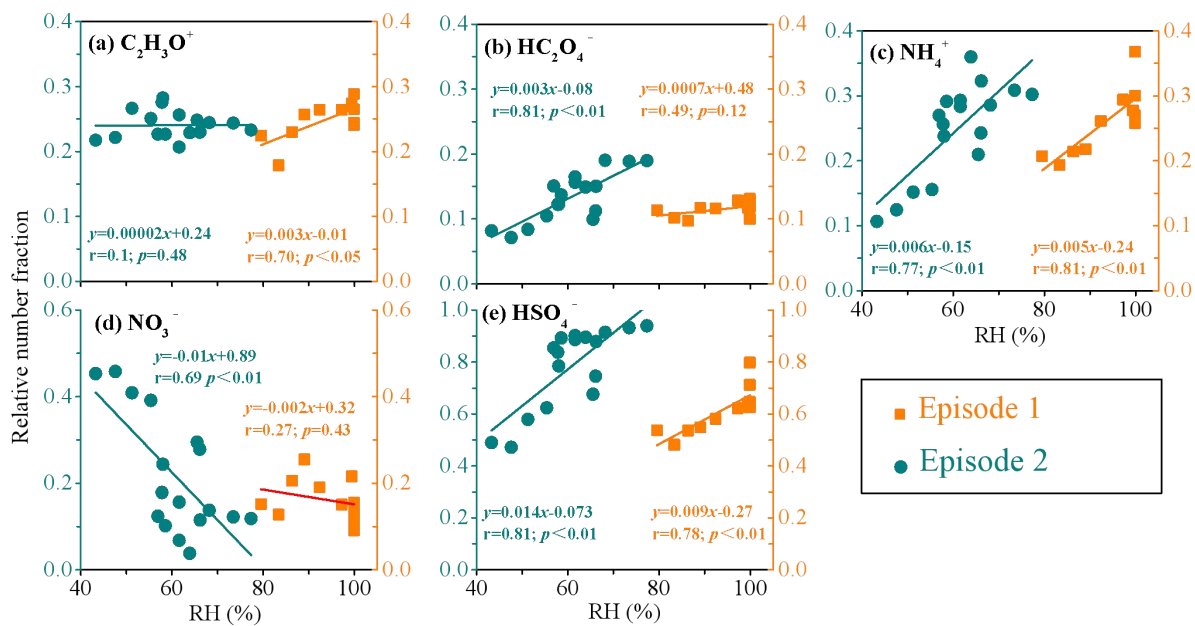
Figure 5. Number fractions of secondary markers associated with the six particle types (i.e., rich-K, BB, OC, Ammonium, EC-aged, and Dust) in four clusters. Secondary markers include sulfate ($^{97}HSO_4^-$), sulfuric acid ($^{195}H(HSO_4)_2^-$), nitrate ($^{62}NO_3^-$), ammonium ($^{18}NH_4^+$), amine ($^{58}C_2H_5NHCH_2^+$), and oxalate ($^{89}HC_2O_4^-$).

884

885 Figure 6. Correlations between the relative number fractions of the secondary species (a) [43]$C_2H_3O^+$, (b)

886 [89]$HC_2O_4^-$, (c) [18]NH_4^+, (d) [62]NO_3^-, (e) [97]HSO_4^- and O_x concentration during E1 (blue square) and E2 (red

887 dot).

Figure 7. Correlations between the relative number fractions of the secondary species (a) [43]$C_2H_3O^+$, (b) [89]$HC_2O_4^-$, (c) [18]NH_4^+, (d) [62]NO_3^-, (e) [97]HSO_4^- and relative humidity (RH) during E1 (cyan dot) and E2 (orange square).